

Received September 4, 2019, accepted October 3, 2019, date of publication October 11, 2019, date of current version October 24, 2019.

Digital Object Identifier 10.1109/ACCESS.2019.2946609

# Combined Quaternion-Based Error State Kalman Filtering and Smooth Variable Structure Filtering for Robust Attitude Estimation

WONKEUN YOUN<sup>ID</sup>, (Member, IEEE), AND  
STEPHEN ANDREW GADSDEN<sup>ID</sup>, (Senior Member, IEEE)

<sup>1</sup> UAV System Division, Aeronautics Research and Development Head Office, Korea Aerospace Research Institute, Daejeon 34133, South Korea

<sup>2</sup> College of Engineering and Physical Sciences, University of Guelph, Guelph, ON N1G 2W1, Canada

Corresponding author: Stephen Andrew Gadsden (gadsden@uoguelph.ca)

This work was supported in part by the Research and Development Project Funded by the Korea Aerospace Research Institute (KARI) under Grant FR19116, and in part by the Natural Sciences and Engineering Research Council of Canada (NSERC) Discovery Grant.

**ABSTRACT** This paper presents a novel robust quaternion-based error state Kalman filter (ESKF) for coping with modeling uncertainty in inertial measurement unit (IMU)-based attitude estimation. The smooth variable structure filter (SVSF) has recently been proposed and proven to be robust to modeling uncertainty. In an effort to combine the accuracy of an ESKF with the robustness of the SVSF, the ESKF and SVSF algorithms have been merged to create the ESKF-SVSF algorithm. In particular, a comprehensive fault detection strategy has been proposed to combine the optimality of the ESKF and the robustness of the SVSF. The proposed ESKF-SVSF algorithm was validated on experimental data collected from a small unmanned aerial vehicle (UAV) in the presence of faulty gyroscope signals. In the experiment, four faulty test cases were considered, involving the injection of two types of faults into the raw gyroscope signals to simulate modeling uncertainty. Although the proposed ESKF-SVSF algorithm incurs a slightly increased computational load, the experimental results demonstrate that the proposed algorithm yields more accurate attitude estimates than the conventional approach does in the presence of modeling uncertainty.

**INDEX TERMS** Attitude estimation, error state Kalman filter, inertial measurement units, modeling uncertainty, quaternion, smooth variable structure filter.

## I. INTRODUCTION

Accurate and reliable attitude estimation is crucial for the safe navigation and control of aerial vehicles [1], ground vehicles [2], underwater vehicles [3], and satellites [4]–[6]. However, sensor and actuator faults may cause critical issues threatening the overall safety of such a vehicle; thus, there is an urgent need for immediate fault identification and isolation [7]. For instance, commercial aircraft are equipped with at least three redundant inertial measurement units (IMUs) to cope with various IMU fault situations [8].

Recently, microelectromechanical system (MEMS)-based IMUs, which typically consist of a 3-axis accelerometer, a 3-axis gyroscope, and a 3-axis magnetometer, have become popular for attitude estimation in various applications due to their light weight, compact size, low power consumption,

The associate editor coordinating the review of this manuscript and approving it for publication was Lubin Chang<sup>ID</sup>.

and low cost [9]. Additionally, these low-cost IMUs have recently enabled related advances in industrial applications of small unmanned aerial vehicles (UAVs). However, unlike in commercial aircraft, redundant IMUs cannot be installed in a small, low-cost UAV due to its limited payload and size to ensure a fault-tolerant system of IMUs.

The well-known Kalman filtering technique has been widely implemented for attitude estimation using IMUs [10]. This technique requires a complete mathematical description of the system and measurement models along with their noise statistics. However, accurate modeling with low-cost IMUs requires a complex, time-consuming process, and the obtained model is inevitably susceptible to an unknown constant bias or a time-varying random bias when an IMU fault occurs. Such malfunctioning of IMUs can cause the estimation performance of the Kalman filter to severely deteriorate or can even cause the filter to diverge. Thus, an appropriate mitigation algorithm for suppressing the effect

of IMU faults is strongly required in the Kalman filtering scheme [11].

In most Kalman filtering approaches for attitude estimation, the attitude is first propagated by integrating the angular rate from the gyroscope to serve as the input signal [12]. The attitude is then updated using the information from the accelerometer and magnetometer. In static or low-dynamics conditions, the accelerometer measures the Earth's gravity and provides information on the roll and pitch, while the magnetometer primarily provides yaw information by measuring the earth's magnetic field [13]. Since the inclination angle of the magnetic field is nonzero except on the Earth's equator, the magnetometer also provides some information on the pitch and roll. Thus, an information fusion procedure using both accelerometer and magnetometer measurements can be used as the measurement update procedure in the Kalman filtering scheme.

However, such an accelerometer-based measurement update procedure is very sensitive to the excessive vibration and external acceleration experienced when a UAV accelerates [14]. In addition, magnetometer measurements can be easily interfered by external magnetic disturbances due to the rotation of the motor or nearby steel bodies [15]. To address the aforementioned cases, several methods, such as covariance adaptation [16], adaptive Kalman filtering [17] and an adaptive cost function [18], have been successfully proposed. The basic principle underlying these filtering schemes is to adaptively compute the relative weights of the information obtained from the gyroscope-based predictions and the measurement update of the accelerometer/magnetometer by adjusting the measurement covariance.

However, the aforementioned approach often requires a large number of data samples for detecting disturbances [19], thus leading to slow response times and large estimation errors. In addition, these algorithms focus only on the case of accelerometer/magnetometer measurement faults and do not consider the possibility of a faulty input gyroscope signal. Thus, only gyroscope faults, such as system modeling uncertainty, are considered in this paper, whereas acceleration and magnetic disturbances are beyond the current scope.

Various approaches have been proposed for handling sensor faults in UAV navigation [20]. Many studies have utilized an aerodynamic model of an aircraft as the system model for Kalman filtering [21]. However, the identification of aerodynamic forces and moments is often a complex and time-consuming process and may also be subject to high uncertainty. A kinematic-model-based two-stage Kalman filter has been implemented to simultaneously estimate IMU faults as augmented states [22]. However, for a system with a high-dimensional state space, this approach may incur an additional computational load due to the augmented states, thus making it unsuitable for real-time application, and may lead to a loss of numerical stability, particularly for ill-conditioned systems [23]. In addition, a system model with an unknown time-varying bias due to IMU faults cannot be

readily obtained. Thus, an augmented-state-based approach is not considered in this paper.

As an alternative approach, the smooth variable structure filter (SVSF), introduced in 2007, has been proven to be robust to modeling uncertainty. An extended Kalman filter (EKF) [24], an unscented Kalman filter (UKF) [24], and a cubature Kalman filter (CKF) [25] have all been merged with the SVSF to address modeling uncertainty, and the simulation results demonstrate improved robustness and accuracy of estimation. In contrast to the augmented-state-based approach, the SVSF is relatively easy to implement and incurs only a slight increase in computational complexity [25]. Simulation results obtained using the SVSF have been presented in many previous papers [24]–[26], but few results obtained based on real-world data have been reported.

To the best of our knowledge, several studies have verified robust attitude estimation algorithms for cases of accelerometer/magnetometer measurement faults, whereas very few studies have investigated the feasibility of attitude algorithms that are robust to faults in the angular rate estimates obtained from gyroscope data. The main motivation of this paper is to propose a new robust attitude estimation algorithm called the ESKF-SVFS algorithm, which effectively combines the accuracy of an error state Kalman filter (ESKF) with the robustness of the SVSF. In particular, a comprehensive fault detection strategy has been proposed to effectively switch between the ESKF and SVSF according to the fault diagnosis. The proposed ESKF-SVFS algorithm has been validated on an IMU dataset collected from a UAV in the presence of faults in the angular rate signals from the gyroscope.

This paper is organized as follows. The ESKF for attitude estimation, including sensor modeling and system kinematics, is presented in Section II. In Section III, the SVSF formulation is presented. In Section IV, the proposed comprehensive fault detection strategy is presented. In Section V, the experimental results and discussion are presented. Conclusions and future work are presented in Section VI.

## II. ERROR STATE KALMAN FILTER FOR QUATERNION KINEMATICS FOR ATTITUDE ESTIMATION

An arbitrary orientation can be represented by a unit quaternion as follows:

$$\mathbf{q} = q_w + q_x i + q_y j + q_z k = \begin{bmatrix} q_w \\ \mathbf{q}_v \end{bmatrix} = \begin{bmatrix} \cos(\theta/2) \\ e_x \sin(\theta/2) \\ e_y \sin(\theta/2) \\ e_z \sin(\theta/2) \end{bmatrix} \quad (1)$$

where  $q_w$  is referred to as the real part of the quaternion and  $\mathbf{q}_v = q_x i + q_y j + q_z k$  is the vector part.  $\theta$  is the rotation angle, and  $\bar{\mathbf{e}} = [e_x, e_y, e_z]^T$  is the axis of rotation. Note that Hamilton's quaternion convention, rather than the JPL quaternion convention, is used in this paper.

The quaternion must satisfy the following norm constraint:

$$|\mathbf{q}| = \sqrt{\mathbf{q}^T \mathbf{q}} = \sqrt{q_w^2 + q_x^2 + q_y^2 + q_z^2} = 1 \quad (2)$$

The successive quaternion product operation is defined as

$$\mathbf{p} \otimes \mathbf{q} = \begin{bmatrix} p_w q_w - \mathbf{p}_v^T \mathbf{q}_v \\ p_w \mathbf{q}_v + q_w \mathbf{p}_v + \mathbf{p}_v \times \mathbf{q}_v \end{bmatrix} \quad (3)$$

$$\mathbf{q}^{-1} = [q_w, -\mathbf{q}_v]^T \quad (4)$$

$$\mathbf{q} \otimes \mathbf{q}^{-1} = [1, 0, 0, 0]^T \quad (5)$$

where  $\otimes$  denotes quaternion multiplication and  $\mathbf{q}^{-1}$  is the inverse quaternion of  $\mathbf{q}$ .

The reference frame of the strap-down IMU is referred to as the body-fixed frame  $\{b\}$ . The navigation frame is denoted by  $\{n\}$ . In this paper, the local north-east-down (NED) frame is used as the navigation frame. An arbitrary 3-dimensional vector in the body-fixed frame,  $\mathbf{v}_b$ , can be transformed into the corresponding vector in the navigation frame,  $\mathbf{v}_n$ , as follows:

$$\mathbf{v}_n = \mathbf{R}_b^n(\mathbf{q})\mathbf{v}_b \quad (6)$$

where rotation matrix  $\mathbf{R}_b^n(\mathbf{q}) \in \text{SO}(3)$  represents the relative orientation with respect to the navigation frame as follows:

$$\mathbf{R}_b^n(\mathbf{q}) = \begin{bmatrix} q_w^2 + q_x^2 - q_y^2 - q_z^2 & 2(q_x \cdot q_y - q_w \cdot q_z) \\ 2(q_x \cdot q_y + q_w \cdot q_z) & q_w^2 - q_x^2 + q_y^2 - q_z^2 \\ 2(q_x \cdot q_z - q_w \cdot q_y) & 2(q_y \cdot q_z + q_w \cdot q_x) \\ 2(q_x \cdot q_z - q_w \cdot q_y) & 2(q_y \cdot q_z - q_w \cdot q_x) \\ q_w^2 - q_x^2 - q_y^2 - q_z^2 & \end{bmatrix}. \quad (7)$$

#### A. PROBLEM FORMULATION

Consider the following discrete nonlinear system and measurement models:

$$\begin{aligned} \mathbf{x}_k &= f(\mathbf{x}_{k-1}, \mathbf{u}_k, \mathbf{w}_k) \\ \mathbf{z}_k &= h(\mathbf{x}_k, \mathbf{v}_k) \end{aligned} \quad (8)$$

where  $k$  is the time index,  $\mathbf{x}_k$  is the state,  $\mathbf{u}_k$  is the input, and  $\mathbf{z}_k$  is the measurement.  $f$  and  $h$  are the system and measurement models, respectively. The nonlinear system noise and measurement noise are typically assumed to be white Gaussian noise, such that  $\mathbf{v}_k \sim N(0, \mathbf{Q}_k)$  and  $\mathbf{w}_k \sim N(0, \mathbf{R}_k)$ , respectively, where  $N(\mu, \Sigma)$  denotes a normal distribution with a mean of  $\mu$  and a covariance of  $\Sigma$ .

In comparison to a direct quaternion-based Kalman filter, the ESKF approach has several distinctive advantages. First, the error state system is always relatively small and lies near the origin, thus preventing possible singularities and gimbal lock issues while ensuring the validity of linearization at all times [30]. Moreover, the ESKF approach ensures numerical stability and allows the quaternion to be handled in its minimal representation [31]. Thus, in the algorithm proposed in this paper, an ESKF is used as the base filter, and the robustness of the SVSF is integrated into the measurement update of the ESKF to mitigate the modeling uncertainty.

The basic working principle of an ESKF is to treat the true state ( $\mathbf{x}_t$ ) as a combination of the nominal state ( $\mathbf{x}$ ) and an error state ( $\delta\mathbf{x}$ ), where the error state represents the difference between the nominal state and the true state, thus yielding the following relationship [32]:

$$\mathbf{x}_t = \mathbf{x} \oplus \delta\mathbf{x} \quad (9)$$

where  $\oplus$  denotes the typical addition operation for all state variables  $\in \mathbb{R}^3$  except for the quaternion state. For the quaternion state, the error state is defined in the local frame as follows:

$$\mathbf{q}_t = \mathbf{q} \otimes \delta\mathbf{q} \quad (10)$$

where  $\delta\mathbf{q} = [1, \delta\theta/2]^T$  denotes the attitude error [33].

In the following subsections, the states of the ESKF for attitude estimation are defined in terms of a 10-element true-state vector ( $\mathbf{x}_t$ ), a 10-element nominal-state vector ( $\mathbf{x}$ ), and a 9-element error-state vector ( $\delta\mathbf{x}$ ), as follows:

$$\mathbf{x}_t = [\mathbf{q}_t \ \boldsymbol{\omega}_{bt} \ \mathbf{a}_{bt}]^T \in \mathbb{R}^{10} \quad (11a)$$

$$\mathbf{x} = [\mathbf{q} \ \boldsymbol{\omega}_b \ \mathbf{a}_b]^T \in \mathbb{R}^{10} \quad (11b)$$

$$\delta\mathbf{x} = [\delta\theta \ \delta\boldsymbol{\omega}_b \ \delta\mathbf{a}_b]^T \in \mathbb{R}^9 \quad (11c)$$

where  $\{q_w, q_x, q_y, q_z\} \in \mathbf{q}_t$ ,  $\{\omega_{bx}, \omega_{by}, \omega_{bz}\} \in \boldsymbol{\omega}_{bt}$ , and  $\{a_{bx}, a_{by}, a_{bz}\} \in \mathbf{a}_{bt}$  represent the true quaternion expressed in the navigation frame, the true gyroscope bias, and the accelerometer bias expressed in the body-fixed frame, respectively.

The conversion between Euler angle  $[\phi, \theta, \psi]^T$  and the corresponding quaternion can be summarized as follows:

$$\begin{aligned} \mathbf{q} &= \begin{bmatrix} \cos(\phi/2)\cos(\theta/2)\cos(\psi/2) + \sin(\phi/2)\sin(\theta/2)\sin(\psi/2) \\ \sin(\phi/2)\cos(\theta/2)\cos(\psi/2) - \cos(\phi/2)\sin(\theta/2)\sin(\psi/2) \\ \cos(\phi/2)\sin(\theta/2)\cos(\psi/2) + \sin(\phi/2)\cos(\theta/2)\sin(\psi/2) \\ \cos(\phi/2)\cos(\theta/2)\sin(\psi/2) - \sin(\phi/2)\sin(\theta/2)\cos(\psi/2) \end{bmatrix} \\ \begin{bmatrix} \phi \\ \theta \\ \psi \end{bmatrix} &= \begin{bmatrix} \text{atan2}\left(\frac{2(q_w q_x + q_y q_z)}{1 - 2(q_x^2 + q_y^2)}\right) \\ \text{asin}\left(\frac{2(q_w q_y - q_z q_x)}{\sqrt{1 - 2(q_x^2 + q_y^2)}}\right) \\ \text{atan2}\left(\frac{2(q_w q_z + q_x q_y)}{1 - 2(q_y^2 + q_z^2)}\right) \end{bmatrix}. \end{aligned}$$

#### B. SENSOR MODELING

A typical IMU measures 3-axis accelerations, 3-axis angular rates, and 3-axis magnetic fields with respect to the body-fixed frame. The measurements obtained from an IMU are typically corrupted by white Gaussian noise and slowly varying bias terms. The following model represents the relationship between the measured IMU signals and the true ones. It should be noted that the effects of misalignment and scale factor errors of the IMU are ignored, under the assumption that the effects of these parameters can be reduced through proper calibration.

##### 1) GYROSCOPE

The three-axis gyroscope measures the angular rate about each of three axes, as follows:

$$\boldsymbol{\omega}_m = \boldsymbol{\omega}_t + \boldsymbol{\omega}_{bt} + \boldsymbol{\omega}_n \quad (12)$$

where  $\boldsymbol{\omega}_m \in \mathbb{R}^3$  is the measured angular rate signal,  $\boldsymbol{\omega}_t \in \mathbb{R}^3$  is the true angular rate signal,  $\boldsymbol{\omega}_{bt} \in \mathbb{R}^3$  is a slowly varying bias term for the gyroscope, and  $\boldsymbol{\omega}_n \in \mathbb{R}^3$  is zero-mean Gaussian noise.

## 2) ACCELEROMETER

The accelerometer measures gravity minus acceleration. However, in static or low-dynamics conditions, the dominant factor affecting the accelerometer measurement is gravity, and thus, the measurement can be approximated as follows [17]:

$$\begin{aligned} \mathbf{a}_m &= \mathbf{R}_b^n(\mathbf{q})^T(\mathbf{a}_t - \mathbf{g}) + \mathbf{a}_{bt} + \mathbf{a}_n \\ &\approx \mathbf{R}_b^n(\mathbf{q})^T \cdot \begin{bmatrix} 0 \\ 0 \\ -\mathbf{g}_0 \end{bmatrix} + \mathbf{a}_{bt} + \mathbf{a}_n \\ &= \begin{bmatrix} 2(q_x \cdot q_z - q_w \cdot q_y) \\ 2(q_y \cdot q_z + q_w \cdot q_x) \\ q_w^2 - q_x^2 - q_y^2 - q_z^2 \end{bmatrix} + \mathbf{a}_{bt} + \mathbf{a}_n \quad (13) \end{aligned}$$

where  $\mathbf{a}_m \in \mathbb{R}^3$  is the measured acceleration signal,  $\mathbf{a}_{bt} \in \mathbb{R}^3$  is the true acceleration,  $\mathbf{a}_n \sim N(0, \sigma_a)$  is zero-mean Gaussian noise,  $\mathbf{a}_{bt} \in \mathbb{R}^3$  is a slowly varying accelerometer bias term, and  $\mathbf{g}_0 = [0, 0, 1]^T$  is the true normalized gravitational acceleration in the navigation frame, serving as the unit vector.

## 3) MAGNETOMETER

The 3-axis magnetometer provides measurements of the magnetic field as follows:

$$\begin{aligned} \mathbf{m}_m &= \mathbf{R}_b^n(\mathbf{q})^T \cdot \bar{\mathbf{H}} + \mathbf{m}_n \\ &= \mathbf{R}_b^n(\mathbf{q})^T \cdot \begin{bmatrix} \mathbf{H} \cos(\varphi_{inc}) \cos(\varphi_{dec}) \\ \mathbf{H} \cos(\varphi_{inc}) \sin(\varphi_{dec}) \\ \mathbf{H} \sin(\varphi_{inc}) \end{bmatrix} + \mathbf{m}_n \quad (14) \end{aligned}$$

where  $\mathbf{m}_m \in \mathbb{R}^3$  is the measured magnetic field,  $\mathbf{m}_n \sim N(0, \sigma_m)$  is zero-mean Gaussian noise,  $\bar{\mathbf{H}}$  is the Earth's magnetic field vector expressed in the navigation frame,  $\mathbf{H}$  is the magnitude of the magnetic flux density,  $\varphi_{dec}$  is the declination angle, and  $\varphi_{inc}$  is the inclination angle of the Earth's magnetic field [34]. The last three parameters ( $\mathbf{H}$ ,  $\varphi_{dec}$ , and  $\varphi_{inc}$ ) vary with the geodetic location and time and can be obtained from the World Magnetic Model (WMM) database.

## C. SYSTEM KINEMATICS

In the ESKF formulation, the true-state, nominal-state, and error-state kinematics are addressed. The true-state kinematics, including noise, can be represented as follows [35]:

$$\dot{\mathbf{q}}_t = \frac{1}{2}\mathbf{q}_t \otimes (\boldsymbol{\omega}_m - \boldsymbol{\omega}_{bt} - \boldsymbol{\omega}_n) \quad (15a)$$

$$\dot{\boldsymbol{\omega}}_{bt} = \mathbf{a}_\omega \quad (15b)$$

$$\dot{\mathbf{a}}_{bt} = \mathbf{a}_\omega \quad (15c)$$

where  $\boldsymbol{\omega}_\omega$  and  $\mathbf{a}_\omega$  represent the bias driving noise for the gyroscope and accelerometer, respectively, corresponding to the process noise.

The nominal-state kinematics represents the system dynamics without noise or perturbations and can be expressed as follows:

$$\dot{\mathbf{q}} = \frac{1}{2}\mathbf{q} \otimes (\boldsymbol{\omega}_m - \boldsymbol{\omega}_b) \quad (16a)$$

$$\dot{\boldsymbol{\omega}}_b = 0 \quad (16b)$$

$$\dot{\mathbf{a}}_b = 0 \quad (16c)$$

The linearized dynamics of the error-state kinematics can be obtained by reformulating the true-state equations given in (15) as the corresponding combination of the nominal state as expressed in (16) with an error state and simplifying up to all second-order infinitesimals as follows:

$$\delta\dot{\boldsymbol{\theta}} = -[\boldsymbol{\omega}_m - \boldsymbol{\omega}_b] \times \delta\boldsymbol{\theta} - \delta\boldsymbol{\omega}_b - \boldsymbol{\omega}_n \quad (17a)$$

$$\delta\dot{\boldsymbol{\omega}}_b = \boldsymbol{\omega}_\omega \quad (17b)$$

$$\delta\dot{\mathbf{a}}_b = \mathbf{a}_\omega \quad (17c)$$

where

$$[\mathbf{a}]_\times = \begin{bmatrix} 0 & -a_z & a_y \\ a_z & 0 & -a_x \\ -a_y & a_x & 0 \end{bmatrix} \quad (18)$$

## D. ERROR STATE KALMAN FILTER FORMULATION

The nominal state does not include the noise terms in (15) and is propagated by integrating the nominal kinematics expressed in (16) as follows:

$$\hat{\mathbf{x}}_{k-1}^+ = f(\hat{\mathbf{x}}_{k-1}^-, \mathbf{u}_{k-1}, 0) \quad (19)$$

where the superscripts + and - denote a posteriori and a priori estimates, respectively. The corresponding 10-element nominal-state vector kinematics (in terms of  $\mathbf{q}$ ,  $\boldsymbol{\omega}_b$ , and  $\mathbf{a}_b$ ) is represented as follows:

$$\hat{\mathbf{q}}_k^- = \hat{\mathbf{q}}_{k-1}^+ \otimes \mathbf{q} \{(\boldsymbol{\omega}_m - \boldsymbol{\omega}_b)\Delta t\} \quad (20a)$$

$$\hat{\boldsymbol{\omega}}_{b,k}^- = \hat{\boldsymbol{\omega}}_{b,k-1}^+ \quad (20b)$$

$$\hat{\mathbf{a}}_{b,k}^- = \hat{\mathbf{a}}_{b,k-1}^+ \quad (20c)$$

where  $\Delta t$  denotes the sampling time corresponding to the IMU publishing rate and has an almost constant value of approximately 250 Hz. Linear evolution of  $\boldsymbol{\omega}$  during  $\Delta t$  is assumed. Thus, the first-order quaternion integrator can be implemented as follows [31]:

$$\hat{\mathbf{q}}_k^- = \hat{\mathbf{q}}_{k-1}^+ \otimes \left( q(\bar{\boldsymbol{\omega}}\Delta t) + \frac{\Delta t^2}{24} \begin{bmatrix} 0 \\ \boldsymbol{\omega}_{k-1} \times \boldsymbol{\omega}_k \end{bmatrix} \right) \quad (21)$$

where  $\bar{\boldsymbol{\omega}} = 0.5(\boldsymbol{\omega}_{k+1} + \boldsymbol{\omega}_k)$  is the average angular rate.

The error-state kinematics expressed in (17) can be integrated as follows:

$$\delta\hat{\mathbf{x}}_k^- = \mathbf{F}_{N,k-1}\delta\hat{\mathbf{x}}_{k-1}^+ \quad (22)$$

Generally, the step of predicting the error state  $\delta\hat{\mathbf{x}}_k^-$  as expressed in (22) can be neglected because the value of  $\delta\hat{\mathbf{x}}_k^-$  is initially set to zero and returns to zero. The a priori covariance  $\mathbf{P}_k^-$  is updated as follows:

$$\mathbf{P}_k^- = \mathbf{F}_{N,k-1}\mathbf{P}_{k-1}^+\mathbf{F}_{N,k-1}^T + \mathbf{F}_i\mathbf{Q}_i\mathbf{F}_i^T \quad (23)$$

where  $\mathbf{F}_N$  is the transition matrix and can be obtained via Euler integration of (17) with respect to the error state  $\delta\mathbf{x}$ .

$\mathbf{F}_i$  is the perturbation Jacobian of (17) with respect to the perturbation vector  $i$ , as follows:

$$\mathbf{F}_i = \partial f(x, \cdot) / \partial \omega = \begin{bmatrix} -\mathbf{I}_{3 \times 3} & \mathbf{0}_{3 \times 3} & \mathbf{0}_{3 \times 3} \\ \mathbf{0}_{3 \times 3} & -\mathbf{I}_{3 \times 3} & \mathbf{0}_{3 \times 3} \\ \mathbf{0}_{3 \times 3} & \mathbf{0}_{3 \times 3} & \mathbf{I}_{3 \times 3} \end{bmatrix}$$

where  $\mathbf{Q}_i$  is the covariance matrix of the perturbation impulses, given by

$$\mathbf{Q}_i = \begin{bmatrix} \Theta_i & \mathbf{0}_{3 \times 3} & \mathbf{0}_{3 \times 3} \\ \mathbf{0}_{3 \times 3} & \Omega_i & \mathbf{0}_{3 \times 3} \\ \mathbf{0}_{3 \times 3} & \mathbf{0}_{3 \times 3} & \mathbf{A}_i \end{bmatrix}$$

with

$$\Theta_i = \Omega_n \Delta t^2 = \sigma_{\omega_n}^2 \Delta t^2 \mathbf{I}_{3 \times 3} \quad [\text{rad}^2] \quad (24a)$$

$$\Omega_i = \Omega_\omega \Delta t = \sigma_{\omega_\omega}^2 \Delta t \mathbf{I}_{3 \times 3} \quad [\text{rad}^2/\text{s}^2] \quad (24b)$$

$$\mathbf{A}_i = \mathbf{A}_\omega \Delta t = \sigma_{a_\omega}^2 \Delta t \mathbf{I}_{3 \times 3} \quad [\text{m}^2/\text{s}^4] \quad (24c)$$

where  $\sigma_{\omega_n}^2$  [rad/s],  $\sigma_{\omega_\omega}^2$  [rad/s/ $\sqrt{\text{s}}$ ], and  $\sigma_{a_\omega}^2$  [m/s $^2$ / $\sqrt{\text{s}}$ ] can be determined from the information given in the IMU's specification sheets or through Allen variance analysis [36].

Continuous differential equations of the form  $\dot{x} = f(x, u)$  can be integrated by taking the exponential Taylor series, as follows:

$$\begin{aligned} \mathbf{F}_N &= \sum_{n=0}^{N < \infty} \frac{1}{n!} \mathbf{A}^n \Delta t^n \\ &= \mathbf{I} + \mathbf{A} \Delta t + \frac{1}{2} \mathbf{A}^2 \Delta t^2 + \cdots + \frac{1}{N} \mathbf{A}^N \Delta t^N \\ &\cong \mathbf{I} + \mathbf{A} \Delta t \end{aligned}$$

where  $\mathbf{F}_N$  is approximated only by the first-order term since the sampling time  $\Delta t$  is extremely short.

$$\mathbf{A} = \partial f(x, \cdot) / \partial \delta x = \begin{bmatrix} \Theta & -\mathbf{I}_{3 \times 3} & \mathbf{0}_{3 \times 3} \\ \mathbf{0}_{3 \times 3} & \mathbf{0}_{3 \times 3} & \mathbf{0}_{3 \times 3} \\ \mathbf{0}_{3 \times 3} & \mathbf{0}_{3 \times 3} & \mathbf{0}_{3 \times 3} \end{bmatrix}$$

where

$$\Theta = -[\boldsymbol{\omega}_m - \boldsymbol{\omega}_b]_x$$

The measurement update of the ESKF will be executed whenever valid acceleration and magnetometer measurements are available. The Kalman gain of the ESKF,  $\mathbf{K}_k$ , is calculated as follows:

$$\mathbf{K}_k = \mathbf{P}_k^- \mathbf{H}_k^T (\mathbf{H}_k \mathbf{P}_k^- \mathbf{H}_k^T + \mathbf{R}_k)^{-1} \quad (25)$$

with

$$\mathbf{H}_k = \left. \frac{\partial h}{\partial \delta \mathbf{x}} \right|_{\mathbf{x}} = \left. \frac{\partial h}{\partial \mathbf{x}_t} \right|_{\mathbf{x}} \left. \frac{\partial \mathbf{x}_t}{\partial \delta \mathbf{x}} \right|_{\mathbf{x}} = \mathbf{H}_x \mathbf{X}_{\delta x}$$

where

$$\mathbf{X}_{\delta x} = \begin{bmatrix} \mathbf{Q}_{\delta \theta} & \mathbf{0} \\ \mathbf{0} & \mathbf{I}_{14 \times 15} \end{bmatrix}$$

and, in turn,

$$\mathbf{Q}_{\delta \theta} = \frac{\partial (\mathbf{q} \otimes \delta \mathbf{q})}{\partial \delta \theta} = \left. \frac{\partial (\mathbf{q} \otimes \delta \mathbf{q})}{\partial \delta \mathbf{q}} \right|_{\mathbf{q}} \left. \frac{\partial \delta \mathbf{q}}{\partial \delta \theta} \right|_{\delta \hat{\theta}=0}$$

$$\begin{aligned} &= \left. \frac{\partial ([\mathbf{q}]_L \delta \mathbf{q})}{\partial \delta \mathbf{q}} \right|_{\mathbf{q}} \left. \frac{\partial \begin{bmatrix} 1 \\ \frac{1}{2} \delta \theta \end{bmatrix}}{\partial \delta \theta} \right|_{\delta \hat{\theta}=0} \\ &= [\mathbf{q}]_L \frac{1}{2} \begin{bmatrix} 0 & 0 & 0 \\ 1 & 0 & 0 \\ 0 & 1 & 0 \\ 0 & 0 & 1 \end{bmatrix} \end{aligned}$$

The Jacobian  $\mathbf{H}_x$  with respect to the nominal state can be obtained as follows for the acceleration and magnetic field, respectively:

$$\mathbf{H}_x = \begin{bmatrix} -\mathbf{g}_0 \frac{\mathbf{R}_n^b(\mathbf{q})(1 : 3, 3)}{\partial \mathbf{q}} & \mathbf{0}_{3 \times 3} & \mathbf{I}_{3 \times 3} \end{bmatrix} \quad (26)$$

$$\mathbf{H}_x = \begin{bmatrix} \frac{\partial (\mathbf{R}_n^b(\mathbf{q}) \bar{\mathbf{H}})}{\partial \mathbf{q}} & \mathbf{0}_{3 \times 3} & \mathbf{0}_{3 \times 3} \end{bmatrix} \quad (27)$$

The a posteriori estimate of the error state  $\hat{\mathbf{x}}_k^+$  and the a posteriori covariance  $\mathbf{P}_k^+$  are updated as follows:

$$\hat{\mathbf{x}}_k^+ = \mathbf{K}_k (\mathbf{z}_k - h(\hat{\mathbf{x}}_k^-)) \quad (28)$$

$$\mathbf{P}_k^+ = (\mathbf{I} - \mathbf{K}_k \mathbf{H}_k) \mathbf{P}_k^- \quad (29)$$

After the completion of the ESKF measurement update, the nominal state ( $\mathbf{x}$ ) must be updated through appropriate combination with the a posteriori error state ( $\hat{\mathbf{x}}_k^+$ ), as follows:

$$\hat{\mathbf{x}}_k^+ \leftarrow \hat{\mathbf{x}}_k^- \oplus \hat{\mathbf{x}}_k^+ \quad (30)$$

The update of the corresponding 10-element nominal-state vector with the a posteriori error state can be expressed as follows:

$$\hat{\mathbf{q}}_k^+ = \hat{\mathbf{q}}_k^- \otimes \mathbf{q}\{\delta \hat{\theta}_k^+\} \quad (31a)$$

$$\hat{\omega}_{b,k}^+ = \hat{\omega}_{b,k}^- + \delta \hat{\omega}_k^+ \quad (31b)$$

$$\hat{\mathbf{a}}_{b,k}^+ = \hat{\mathbf{a}}_{b,k}^- + \delta \hat{\mathbf{a}}_k^+ \quad (31c)$$

After the nominal state has been updated with the error state, the mean of the error state  $\hat{\mathbf{x}}_k^+$  becomes zero. To complete the ESKF measurement update, the a posteriori covariance must be updated with this modification:

$$\mathbf{P}_k^+ = \mathbf{G}_k \mathbf{P}_k^+ \mathbf{G}_k^T \quad (32)$$

where

$$\mathbf{G}_k = \left. \frac{\partial g}{\partial \delta \mathbf{x}} \right|_{\delta \hat{\mathbf{x}}^+} = \begin{bmatrix} \mathbf{I} - \left[ \frac{1}{2} \delta \hat{\theta}_k^+ \right] \times & \mathbf{0} \\ \mathbf{0} & \mathbf{I}_{6 \times 6} \end{bmatrix}.$$

Notably, the operation expressed in (31a) in particular may induce the violation of the quaternion normalization constraint given in (2) as a result of linearization and arithmetic errors. To avoid such a case, a brute-force quaternion normalization operation must be performed if the discrepancy with respect to the unit quaternion is greater than some small proportion of the noise level (say  $10^{-7}$ ) [37].

$$\hat{\mathbf{q}}_k^+ = \frac{\hat{\mathbf{q}}_k^+}{|\hat{\mathbf{q}}_k^+|} \quad (33)$$

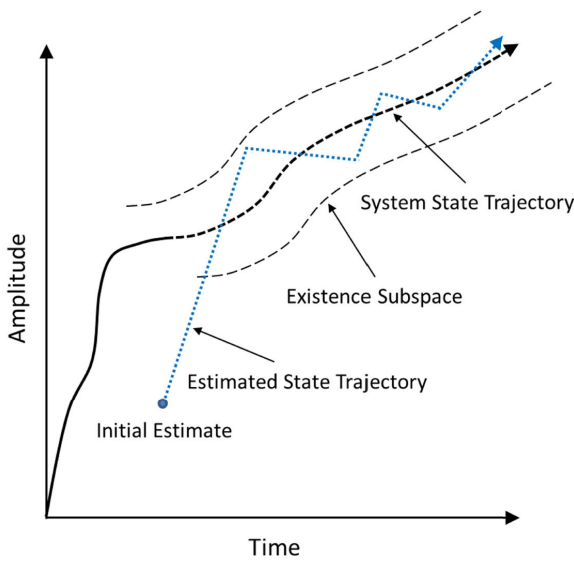


**FIGURE 1.** Concept of SVSF estimation [24].

**TABLE 1.** Comprehensive fault detection strategy.

Case	Chi-square	SPRT	Angle	Diagnosis
1	F	F	F	F
2	F	F	N	F
3	F	N	F	F
4	F	N	N	N
5	N	F	F	F
6	N	F	N	F
7	N	N	F	N
8	N	N	N	N

\*Angle denotes the fault detection result of the angle-deviation-based fault detection.

\*F and N denote the fault and normal status, respectively.

### III. SMOOTH VARIABLE STRUCTURE FILTER

The basic formulation of the SVSF, which has a predictor-corrector structure, was first introduced in 2007 [38] [39] and is inspired by sliding mode control and observer techniques. The SVSF ensures that the estimated state remains in the so-called existing subspace around the true-state trajectory by means of a discontinuous gain, as shown in Fig. 1. The SVSF approach has been proven to be reliable and robust against system modeling and noise uncertainties [40] [41] and [42]. Essentially, the SVSF approach can be applied to any model-based differential linear and/or nonlinear equations. The SVSF strategy consists of recursive prediction and update stages, similar to the Kalman filtering approach, and can be summarized as follows [26]:

$$\hat{\mathbf{x}}_{k+1}^- = f(\hat{\mathbf{x}}_k^+, \mathbf{u}_k) \quad (34)$$

$$\mathbf{P}_{k+1}^- = \mathbf{F}_k \mathbf{P}_k^+ \mathbf{F}_k^T + \mathbf{Q}_k \quad (35)$$

---

#### Algorithm 1 Proposed ESKF-SVFS Algorithm

---

**Input:**  $\omega_m$

**Measurements:**  $\mathbf{a}_m, \mathbf{m}_m$

**Initialization:**  $\hat{\mathbf{q}}_0, \hat{\omega}_{b,0}, \hat{\mathbf{a}}_{b,0}$

**Time update:**

1. Propagate the nominal state

$$\hat{\mathbf{x}}_{k+1}^- = f(\hat{\mathbf{x}}_k^+, \mathbf{u}_{k-1}, 0)$$

2. Propagate the error state

$$\delta\hat{\mathbf{x}}_{k+1}^- = \mathbf{F}_{N,k} \delta\hat{\mathbf{x}}_k^+$$

3. Compute the a priori error covariance

$$\mathbf{P}_{k+1}^- = \mathbf{F}_{N,k} \mathbf{P}_k^+ \mathbf{F}_{N,k}^T + \mathbf{F}_i \mathbf{Q}_i \mathbf{F}_i^T$$

**Measurement update:**

4. Run the chi-square fault detection via (50) - (51)

5. Run the SPRT fault detection  
via (52) - (56)

6. Run the estimate difference fault detection  
via (57) - (58)

7. Run the comprehensive fault detection strategy  
via Table 1

**if diagnosis = F then**

8. Compute the SVSF gain

$$\mathbf{K}_{k+1} = \mathbf{H}_{k+1}^+ \text{diag} \left[ \left( |\mathbf{e}_{z,k+1}^-| + \gamma |\mathbf{e}_{z,k}^+| \right) \circ \text{sat} \left( \bar{\boldsymbol{\psi}}^{-1} \mathbf{e}_{z,k+1}^- \right) \right] \text{diag} \left( \mathbf{e}_{z,k+1}^- \right)^{-1}$$

9. Compute the a posteriori error state

$$\delta\hat{\mathbf{x}}_{k+1}^+ = \mathbf{K}_{k+1} (\mathbf{z}_{k+1} - h(\hat{\mathbf{x}}_{k+1}^-))$$

10. Update the a posteriori nominal state with the  
a posteriori error state

$$\mathbf{x} \leftarrow \mathbf{x} \oplus \delta\hat{\mathbf{x}}_{k+1}^+$$

11. Renormalize the quaternion

$$\hat{\mathbf{q}}_k^+ = \frac{\hat{\mathbf{q}}_k^+}{|\hat{\mathbf{q}}_k^+|}$$

12. Compute the a posteriori error covariance

$$\mathbf{P}_{k+1}^+ = (\mathbf{I} - \mathbf{K}_{k+1} \mathbf{H}_{k+1}) \mathbf{P}_{k+1}^- (\mathbf{I} - \mathbf{K}_{k+1} \mathbf{H}_{k+1})^T + \mathbf{K}_{k+1} \mathbf{R}_{k+1} \mathbf{K}_{k+1}^T$$

13. Update the a posteriori error covariance

$$\mathbf{P}_{k+1}^+ = \mathbf{G}_{k+1} \mathbf{P}_{k+1}^+ \mathbf{G}_{k+1}^T$$

14. Compute the a posteriori innovation

$$\mathbf{e}_{z,k+1}^+ = \mathbf{z}_{k+1} - \hat{\mathbf{z}}_{k+1}^+$$

**else if diagnosis = N**

15. Compute the Kalman gain

$$\mathbf{K}_{k+1} = \mathbf{P}_{k+1}^- \mathbf{H}_{k+1}^T (\mathbf{H}_{k+1} \mathbf{P}_{k+1}^- \mathbf{H}_{k+1}^T + \mathbf{R}_{k+1})^{-1}$$

16. Run steps 9 - 13
- 

where

$$\mathbf{F}_k = \frac{\partial f}{\partial x} \Big|_{\hat{\mathbf{x}}_k^-, \mathbf{u}_k} \quad (36)$$

An a priori innovation  $\mathbf{e}_{z,k+1}^-$  can be calculated from the corresponding predicted measurement  $\hat{\mathbf{z}}_{k+1}^-$  as follows:

$$\hat{\mathbf{z}}_{k+1}^- = h(\hat{\mathbf{x}}_{k+1}^-) \quad (37)$$

$$\mathbf{e}_{z,k+1}^- = \mathbf{z}_{k+1} - \hat{\mathbf{z}}_{k+1}^- \quad (38)$$

The distinctive difference between the Kalman and SVSF approaches is how the gain is formulated. The SVSF gain can



**FIGURE 2.** UAV system used in the experiment.

be expressed as a function of the a priori and a posteriori innovations  $\mathbf{e}_{z,k+1}^-$  and  $\mathbf{e}_{z,k}^+$ , the smoothing boundary layer width  $\psi$ , and the SVSF convergence rate  $\gamma$ , as follows:

$$\mathbf{K}_{k+1} = \mathbf{H}_{k+1}^+ \text{diag} \left[ \left( \left| \mathbf{e}_{z,k+1}^- \right| + \gamma \left| \mathbf{e}_{z,k}^+ \right| \right) \circ \text{sat} \left( \bar{\psi}^{-1} \mathbf{e}_{z,k+1}^- \right) \right] \text{diag} \left( \mathbf{e}_{z,k+1}^- \right)^{-1} \quad (39)$$

Here,  $\circ$  and the superscript  $+$  denote Schur multiplication and the pseudoinverse of a matrix, respectively.  $\bar{\psi}^{-1}$  is a diagonal matrix constructed from the smoothing boundary layer width  $\psi$  and is defined as follows:

$$\bar{\psi}^{-1} = \begin{bmatrix} \frac{1}{\psi_1} & 0 & 0 \\ 0 & \ddots & 0 \\ 0 & 0 & \frac{1}{\psi_m} \end{bmatrix} \quad (40)$$

The measurement Jacobian  $\mathbf{H}_{k+1}$  in (39) is defined as follows:

$$\mathbf{H}_{k+1} = \left. \frac{\partial h}{\partial \mathbf{x}} \right|_{\hat{\mathbf{x}}_{k+1}^-, \mathbf{u}_k} \quad (41)$$

The saturation function in (39) is expressed as shown in the following equation:

$$\text{sat} \left( \bar{\psi}^{-1} \mathbf{e}_{z,k+1}^- \right) = \begin{cases} 1, & \mathbf{e}_{z,k+1}^- / \psi_i \geq 1 \\ \mathbf{e}_{z,k+1}^- / \psi_i, & -1 < \mathbf{e}_{z,k+1}^- / \psi_i \leq 1 \\ -1, & \mathbf{e}_{z,k+1}^- / \psi_i \leq -1 \end{cases} \quad (42)$$

Then, the a posteriori error covariance  $\mathbf{P}_{k+1}^+$  can be computed as follows:

$$\mathbf{P}_{k+1}^+ = (\mathbf{I} - \mathbf{K}_{k+1} \mathbf{H}_{k+1}) \mathbf{P}_{k+1}^- (\mathbf{I} - \mathbf{K}_{k+1} \mathbf{H}_{k+1})^T + \mathbf{K}_{k+1} \mathbf{R}_{k+1} \mathbf{K}_{k+1}^T \quad (43)$$

For utilization in later iterations when calculating the SVSF gain given in (39), the updated measurement estimate  $\hat{\mathbf{z}}_{k+1}^+$  and the a posteriori innovation  $e_{z,k+1}^+$  are computed as follows:

$$\hat{\mathbf{z}}_{k+1}^+ = h(\hat{\mathbf{x}}_{k+1}^+) \quad (44)$$

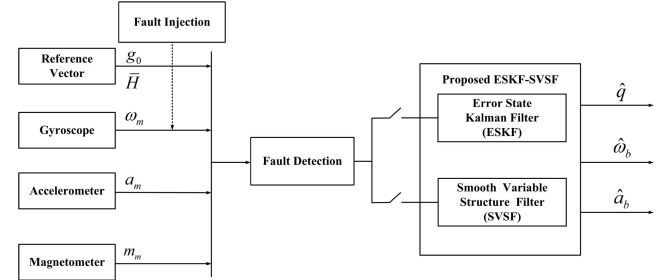


**FIGURE 3.** The proposed ESKF-SVFS algorithm concept. The reference vectors  $\mathbf{g}_0$  and  $\mathbf{H}$  are the true normalized gravitational acceleration and geomagnetic vectors, respectively, in the navigation frame.  $\omega_m$ ,  $\mathbf{a}_m$  and  $\mathbf{m}_m$  are the measured angular rate from the gyroscope, the measured acceleration from the accelerometer, and the measured magnetic field from the magnetometer, respectively. Artificial faults were injected into the raw angular rate signal.

**TABLE 2.** Detailed sensor data specifications for the measurement noise.

Sensor	Specifications
Accelerometer	Output rate: 250 Hz, $\sigma_a = 0.2 \text{ m/s}^2$
Magnetometer	Output rate: 10 Hz, $\sigma_m = 0.05 \text{ gauss}$

$$\mathbf{e}_{z,k+1}^+ = \mathbf{z}_{k+1} - \hat{\mathbf{z}}_{k+1}^+ \quad (45)$$

Note that the estimation performance of the SVSF approach under the normal condition is not optimal, although the SVSF exhibits robustness in the presence of a system fault [24]. Therefore, it is beneficial to combine both the optimality of ESKF and the robustness of SVSF. To address the above issues, the concept of the varying smoothing boundary layer (VBL) has recently been proposed, yielding the new SVSF-VBL algorithm [24]. Specifically, under normal operating conditions when no system fault is detected, the SVSF-VBL algorithm utilizes standard KF gains. Conversely, in the presence of a system fault, the SVSF-VBL utilizes the robust SVSF gain in (39).

The VBL can be obtained by minimizing the trace of the a posteriori covariance with respect to the smoothing boundary layer term  $\psi$  as follows [24]:

$$\frac{\delta (\text{trace}[\mathbf{P}_{k+1}^+])}{\delta \psi} = 0 \quad (46)$$

Then, the VBL solution can be obtained by

$$\psi = \left( \bar{\mathbf{A}}^{-1} \mathbf{H}_{k+1} \mathbf{P}_{k+1}^- \mathbf{H}_{k+1}^T \mathbf{S}_{k+1}^{-1} \right)^{-1} \quad (47)$$

where

$$\mathbf{S}_k = \mathbf{H}_{k+1} \mathbf{P}_{k+1}^- \mathbf{H}_{k+1}^T + \mathbf{R}_{k+1} \quad (48)$$

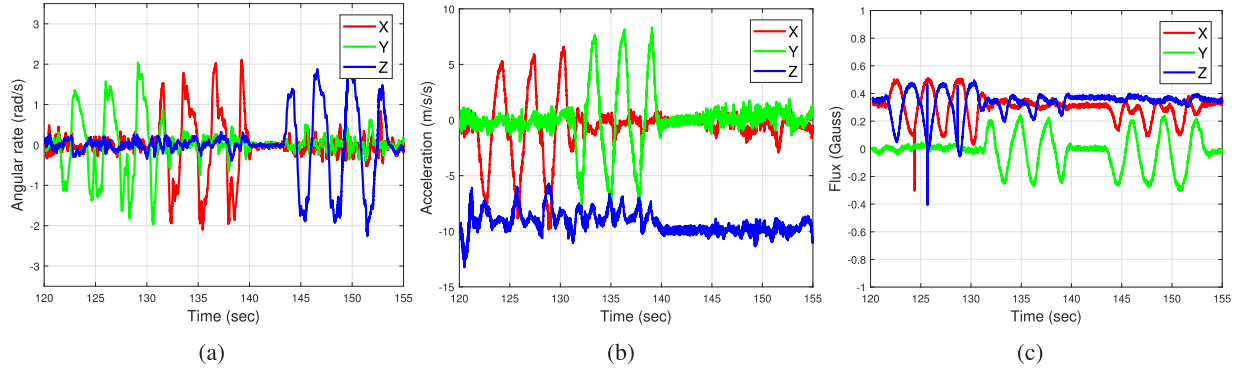
and

$$\mathbf{A} = \left( \left| \mathbf{e}_{z,k+1}^- \right| + \gamma \left| \mathbf{e}_{z,k}^+ \right| \right) \quad (49)$$

The SVSF-VBL algorithm results in a better estimation result since the VBL can provide a continuous indication of the detected system fault. Thus, the SVSF-VBL algorithm switches to the conventional Kalman filter when  $\psi$  exceeds a certain threshold, meaning that there is a system fault. However, it has been reported that the SVSF-VBL algorithm

**TABLE 3.** Detailed sensor data specifications obtained using the Allen variance for the process noise.

Accelerometer	Specifications		
	X	Y	Z
Bias instability ( $\sigma_{\mathbf{a}_n}^2$ [m/s <sup>2</sup> ])	$5.7502 \cdot 10^{-4}$	$4.8152 \cdot 10^{-4}$	$9.7731 \cdot 10^{-4}$
Velocity random walk ( $\sigma_{\mathbf{a}_\omega}^2$ [m/s <sup>2</sup> /√s])	0.0014	0.0015	0.0024
Gyroscope	Specifications		
	X	Y	Z
Bias instability ( $\sigma_{\omega_n}^2$ [rad/s])	$4.7124 \cdot 10^{-5}$	$4.7124 \cdot 10^{-5}$	$3.6652 \cdot 10^{-5}$
Angular random walk ( $\sigma_{\omega_\omega}^2$ [rad/s/√s])	$1.1868 \cdot 10^{-4}$	$1.1694 \cdot 10^{-4}$	$1.1694 \cdot 10^{-4}$

**FIGURE 4.** (a) Raw acceleration signals. (b) Raw angular rate signals. (c) Raw magnetic field signals.

may not be applicable to all engineering applications [44]. In certain applications, the VBL cannot present a reliable indication of system faults; thus, the SVSF-VBL algorithm cannot switch to the robust SVSF gain in the presence of a system fault. Without appropriately switching to the robust SVSF gain, the SVSF-VBL eventually fail to track the accurate state under a system fault.

The multiple model adaptive estimator (MMAE)-based fault detection algorithm has recently been proposed to identify system faults [44]. However, the MMAE runs in a parallel filter, introducing computational burden. In addition, selecting the appropriate subfilter model to detect system faults is unrealistic in practical engineering applications. Alternatively, the interacting multiple model (IMM) filter can be utilized to address the aforementioned issue, but the IMM filter, which consists of a number of subfilters corresponding to different fault models, incurs a substantial computational burden [43]. Therefore, to address the aforementioned problem, we propose an alternative algorithm for the SVSF-VBL based on a comprehensive fault detection strategy.

#### IV. FAULT DETECTION ALGORITHM

Note that the estimation performance of the ESKF will surpass that of the SVSF when there is no modeling uncertainty.

**TABLE 4.** Four faulty test cases.

Scenario	Fault Type	Magnitude of Fault Bias	Occurrence Times
Scenario 1	Constant bias (Case 1)	$\omega_m \leftarrow \omega_m + [2, 2, 2]^T$	124 s, 136 s, 148 s
	Random bias (Case 2)	$\omega_m \leftarrow \omega_m + \sqrt{5} \cdot \text{rand}(3, 1)$	124 s, 136 s, 148 s
Scenario 2	Constant bias (Case 3)	$\omega_m \leftarrow \omega_m + [1, 1, 0.5]^T$	132 s ~ 141 s
	Random bias (Case 4)	$\omega_m \leftarrow \omega_m + \sqrt{2} \cdot \text{rand}(3, 1)$	132 s ~ 141 s

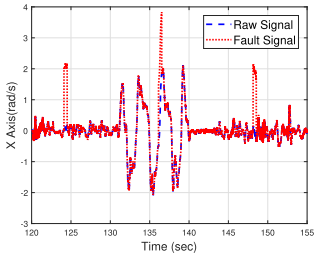
Thus, our strategy is to utilize the output of the ESKF in the absence of a system fault and the SVSF in the presence of a system fault, which may result in a better estimation result. To achieve the aforementioned strategy, accurate fault detection is highly required.

##### A. CHI-SQUARE-BASED FAULT DETECTION

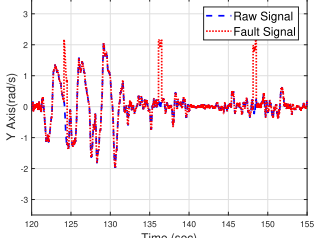
The statistical parameter for measurement fault detection can be defined as follows [27], [28]:

$$\bar{\mathbf{e}}_k = \mathbf{v}_k^T \mathbf{P}_{zz,k}^{-1} \mathbf{v}_k \quad (50)$$

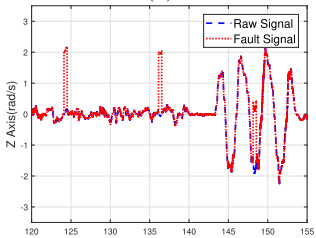
where  $\mathbf{v}_k = \mathbf{z}_k - h(\hat{\mathbf{x}}_k^-)$  and  $\mathbf{P}_{zz,k} = \mathbf{H}_k \mathbf{P}_k^- \mathbf{H}_k^T + \mathbf{R}_k$  are the innovation sequence and innovation covariance, respectively. The hypothesis test for evaluating system failure based on the



(a)



(b)



(c)

**FIGURE 5.** Comparison between the raw and faulty angular rate signals in the experiment (Faulty Case 1, Scenario 1): (a) x-axis, (b) y-axis, and (c) z-axis.

chi-square fault detection is as follows [29]:

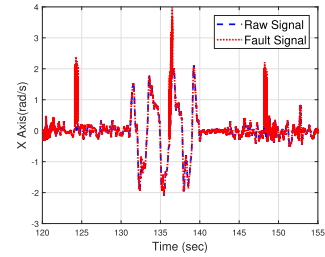
$$\begin{cases} H_0 : \bar{\epsilon}_k < \lambda & \text{Normal} \\ H_1 : \bar{\epsilon}_k \geq \lambda & \text{Fault} \end{cases} \quad (51)$$

where  $\lambda$  can be determined based on a desired confidence level of the chi-square distribution. In this paper, a 95% confidence level was utilized. The chi-square-based fault detection is suitable for detecting sudden system errors, but it is not adequate for detecting a slowly increasing or constant-level system fault.

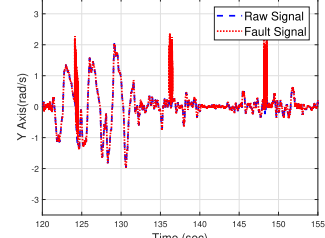
#### B. SPRT-BASED FAULT DETECTION

In contrast to the chi-square fault detection, the SPRT-based fault detection is the statistical hypothesis test for sequential datasets and can identify slowly increasing or constant-level system faults [27]. Utilizing the sequential dataset of the innovation sequence, the binary hypothesis test for evaluating system failure can be expressed as follows:

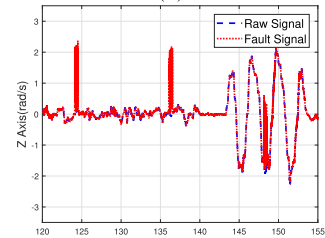
$$\begin{cases} H_0 : p(\mathbf{v}_j | H_0) = \frac{1}{2\pi^{n/2}\mathbf{P}_{zz,j}^{1/2}} \exp \left[ -0.5\mathbf{v}_j^T \mathbf{P}_{zz,j}^{-1} \mathbf{v}_j \right] \\ H_1 : p(\mathbf{v}_j | H_1) = \frac{1}{2\pi^{n/2}\mathbf{P}_{zz,j}^{1/2}} \exp \left[ -0.5(\mathbf{v}_j - \boldsymbol{\mu}_j)^T \mathbf{P}_{zz,j}^{-1} (\mathbf{v}_j - \boldsymbol{\mu}_j) \right] \end{cases} \quad (52)$$



(a)



(b)



(c)

**FIGURE 6.** Comparison between the raw and faulty angular rate signals in the experiment (Faulty Case 2, Scenario 1): (a) x-axis, (b) y-axis, and (c) z-axis.

Then, the likelihood ratio according to the maximum posteriori probability can be obtained by

$$L_k = \frac{p(v_1, \dots, v_k | H_1)}{p(v_1, \dots, v_k | H_0)} = \prod_{j=1}^k \frac{p(v_j | H_1)}{p(v_j | H_0)} \quad (53)$$

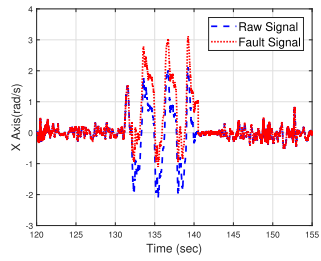
Performing the logarithmic transformation on (53), a logarithmic likelihood ratio can be obtained in the recursive formulation as follows:

$$\begin{aligned} \Lambda_k &= \ln [L_k] = \ln \left[ \prod_{j=1}^k \frac{p(v_j | H_1)}{p(v_j | H_0)} \right] \\ &= \ln \left[ \prod_{j=1}^{k-1} \frac{p(v_j | H_1)}{p(v_j | H_0)} \right] + \ln \left[ \frac{p(v_k | H_1)}{p(v_k | H_0)} \right] = \Lambda_{k-1} + \Delta \Lambda_k. \end{aligned} \quad (54)$$

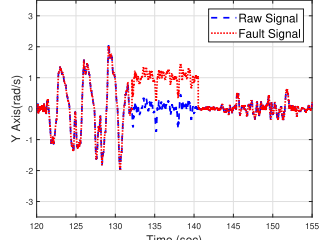
According to the Wald method [45], the threshold value  $T_{sprt}$  can be determined by

$$T_{sprt} = \ln \left( \frac{1 - p_m}{p_f} \right) \quad (55)$$

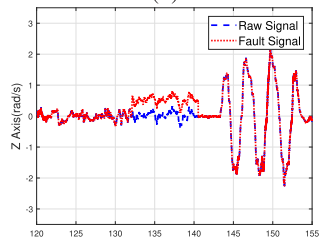
where  $p_m$  and  $p_f$  denote the missed and false alarm rates, respectively.



(a)



(b)



(c)

**FIGURE 7.** Comparison between the raw and faulty angular rate signals in the experiment (Faulty Case 3, Scenario 2): (a) x-axis, (b) y-axis, and (c) z-axis.

Then, the hypothesis test for evaluating system failure based on the SPRT-based fault detection is as follows:

$$\begin{cases} H_0 : \Lambda_k < T_{spkt} & \text{Normal} \\ H_1 : \Lambda_k \geq T_{spkt} & \text{Fault} \end{cases} \quad (56)$$

To prevent unwanted accumulated values beyond the threshold, the feedback reset algorithm is implemented to reset  $\Lambda_k$  to zero after the detected fault ceases [27].

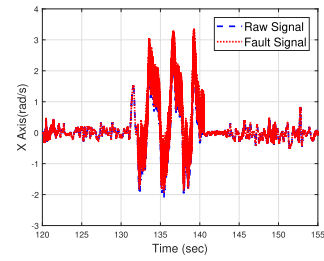
### C. ANGLE-DEVIATION-BASED FAULT DETECTION

The angle deviation obtained by the ESKF and SVSF can be used to detect the modeling uncertainty because the ESKF only yields a stable estimation result in the absence of a system fault, while the SVSF always yields a stable estimation, although it is not the optimal solution in the absence of a system fault. The absolute difference of the Euler angle estimation can be expressed as follows:

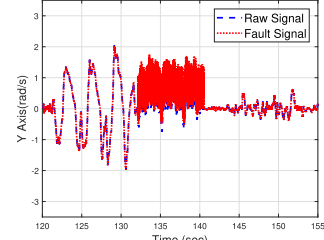
$$|\alpha_k - \hat{\alpha}_k| = |(\phi_k + \theta_k + \psi_k) - (\hat{\phi}_k + \hat{\theta}_k + \hat{\psi}_k)| \quad (57)$$

$$\begin{cases} H_0 : |\alpha_k - \hat{\alpha}_k| < T_{est} & \text{Normal} \\ H_1 : |\alpha_k - \hat{\alpha}_k| \geq T_{est} & \text{Fault} \end{cases} \quad (58)$$

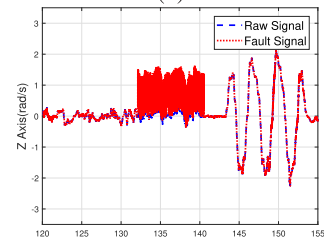
where  $\alpha_k$  and  $\hat{\alpha}_k$  denote the summation of the Euler angle estimate obtained by the ESKF and SVSF, respectively.  $T_{est}$



(a)



(b)



(c)

**FIGURE 8.** Comparison between the raw and faulty angular rate signals in the experiment (Faulty Case 4, Scenario 2): (a) x-axis, (b) y-axis, and (c) z-axis.

denotes the threshold for the angle difference. Note that the  $|\alpha_k - \hat{\alpha}_k|$  parameter may have no statistical significance, but it can be utilized as one of the parameters to detect system faults.

### D. COMPREHENSIVE FAULT DETECTION STRATEGY

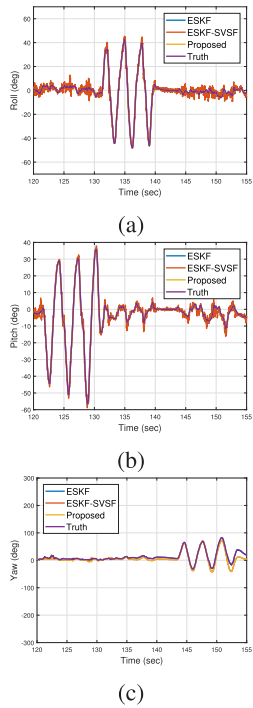
As discussed above, the chi-square-, SPRT-, and angle-deviation-based fault detection strategies have their advantages and disadvantages; thus, it is important to combine these different methods to accurately find system faults. By combining the shortcomings and advantages of these three methods, an integrated fault detection diagnosis strategy can be summarized as shown in Table 1. The proposed approach effectively merges the ESKF and SVSF estimation methods, yielding the novel ESKF-SVSF algorithm, as summarized in Algorithm 1. In summary, the novel ESKF-SVSF algorithm switches to the SVSF when a fault is detected, and vice versa.

### V. EXPERIMENT

To validate the proposed ESKF-SVSF algorithm, an experiment was conducted using a small UAV platform with a MEMS-based IMU, as shown in Fig. 2. The IMU consists of an LSM303D integrated accelerometer/magnetometer unit and an L3GD20 gyroscope. The update rates of the

**TABLE 5.** Performance comparison between the ESKF, ESKF-SVSF, and ESKF-SVSF (proposed) algorithms for the normal case and the four faulty cases (all values expressed in units of degrees).

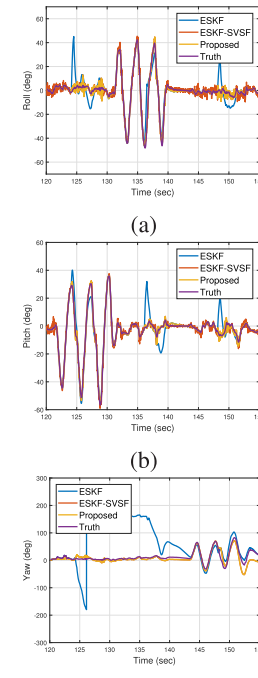
Algorithm	Normal Case			Faulty Case 1			Faulty Case 2		
	ESKF	ESKF-SVSF	ESKF-SVSF (proposed)	ESKF	ESKF-SVSF	ESKF-SVSF (proposed)	ESKF	ESKF-SVSF	ESKF-SVSF (proposed)
RMSE (roll)	1.42	2.35	1.42	6.61	2.04	1.40	3.38	2.03	1.17
AAVB (roll)	1.19	1.78	1.19	3.01	1.51	0.78	1.49	1.50	0.60
MAE (roll)	1.87	9.09	1.87	13.60	10.56	10.43	7.69	10.54	9.89
RMSE (pitch)	0.74	1.72	0.74	5.64	1.60	1.20	2.96	1.59	0.95
AAVB (pitch)	0.56	1.25	0.56	2.54	1.17	0.73	1.33	1.17	0.56
MAE (pitch)	2.15	10.48	2.15	18.43	10.66	6.18	8.45	10.67	4.44
RMSE (yaw)	5.83	6.87	5.83	89.92	12.81	12.73	68.06	10.77	9.34
AAVB (yaw)	4.12	6.62	4.12	62.04	8.63	8.23	54.21	7.33	6.23
MAE (yaw)	9.59	14.28	9.59	184.03	38.30	28.10	132.31	33.27	15.23
Faulty Case 3									
Algorithm	ESKF	ESKF-SVSF	ESKF-SVSF (proposed)	ESKF	ESKF-SVSF	ESKF-SVSF (proposed)	ESKF	ESKF-SVSF	ESKF-SVSF (proposed)
RMSE (roll)	4.44	2.07	1.28	3.04	2.06	1.21			
AAVB (roll)	1.53	1.53	0.62	1.08	1.53	0.57			
MAE (roll)	15.3	10.52	10.37	10.62	10.52	10.23			
RMSE (pitch)	4.59	1.62	0.76	3.32	1.60	0.74			
AAVB (pitch)	1.56	1.22	0.38	1.19	1.12	0.35			
MAE (pitch)	21.61	10.67	6.20	15.22	10.61	6.19			
RMSE (yaw)	47.11	15.94	13.34	44.72	20.90	17.12			
AAVB (yaw)	28.90	12.15	11.23	27.91	15.33	11.32			
MAE (yaw)	127.68	35.68	28.45	121.93	49.10	32.12			

**FIGURE 9.** Attitude estimation results for the normal case: (a) roll, (b) pitch, and (c) yaw.

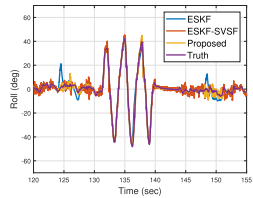
accelerometer and magnetometer are 250 Hz and 10 Hz, respectively. A one-hour static experiment was conducted to analyze the Allan variance, and the measurement noise and process noise of the sensors are summarized in Tables 2 and 3, respectively.

The full states of the GPS/INS Kalman filter, including the position, velocity, attitude, angular rate bias, and acceleration bias, were obtained on the same experimental data and used as our best estimates of the true attitude [35]. Fig. 4(a), (b), and (c) show the raw gyroscope, accelerometer, and magnetometer outputs, respectively, during the experiment.

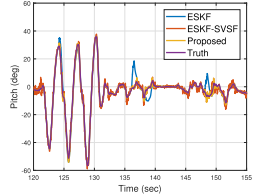
To demonstrate the validity of the proposed ESKF-SVSF algorithm in the presence of modeling uncertainty, four

**FIGURE 10.** Attitude estimation results for Faulty Case 1 (Scenario 1): (a) roll, (b) pitch, and (c) yaw.

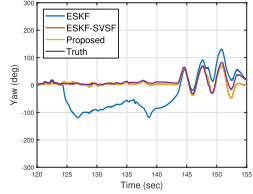
different faulty test cases, involving fault injection with a short time duration (Scenario 1) and with a long time duration (Scenario 2), were investigated, as summarized in Table 4. The use of the IMU signals in the ESKF-SVSF algorithm is illustrated in Fig. 3. In each scenario, two types of faults, namely, constant and random gyroscope faults, were injected into the raw gyroscope data from the experiment to simulate modeling uncertainty. Figs. 5 and 6 show the raw and faulty gyroscope signals for Cases 1 and 2, respectively, corresponding to Scenario 1. The fault occurrence times are 124 s, 136 s, and 148 s, each with a time duration of 0.5 s. Figs. 7 and 8 show the raw and faulty gyroscope signals for Cases 3 and 4, respectively, corresponding to



(a)



(b)



(c)

**FIGURE 11.** Attitude estimation results for Faulty Case 2 (Scenario 1): (a) roll, (b) pitch, and (c) yaw.

Scenario 2. Here, the time interval for fault injection is 132–141 s.

The filters were programmed and implemented using MATLAB 2017b on a PC with an Intel Core i7-6500U CPU operating at 2.50 GHz. The root mean square errors (RMSEs), averaged absolute values of bias (AAVBs), and maximum absolute errors (MAEs) of attitude estimation are presented to evaluate the performance of the proposed algorithm. The AAVB metric is generally used to analyze the bias of state estimates [46]. That is, a smaller AAVB indicates a higher probability that the state estimates will be unbiased.

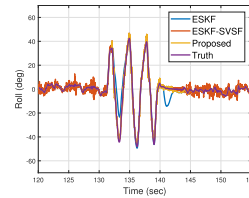
$$\text{RMSE} = \sqrt{\frac{1}{T} \sum_{k=1}^T (\mathbf{x}_k - \hat{\mathbf{x}}_k)^2} \quad (59)$$

$$\text{AAVB} = \frac{1}{T} \sum_{k=1}^T |\mathbf{x}(k) - \hat{\mathbf{x}}(k)| \quad (60)$$

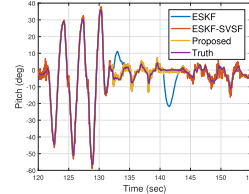
$$\text{MAE} = \max_k(|\mathbf{x}(k) - \hat{\mathbf{x}}(k)|) \quad (61)$$

The constant smoothing boundary layer widths for the SVSF were set to  $\psi = [0.1, 0.1, 0.08]^T$  and  $\psi = [0.2, 0.2, 0.1]^T$  for the accelerometer and magnetometer measurements, respectively. The SVSF convergence rate  $\gamma$  was set to 0.1. These parameters were chosen empirically to minimize the estimation error based on the system/measurement noise statistics.

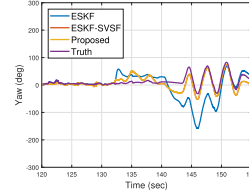
The RMSEs, AAVBs, and MAEs of the roll, pitch, and yaw angles obtained by the ESKF and ESKF-SVFS algorithms for the normal case and the four faulty test cases are summarized in Table 5. Fig. 9(a), (b), and (c) show the attitude estimation results of the ESKF and ESKF-SVFS algorithms



(a)

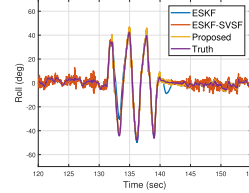


(b)

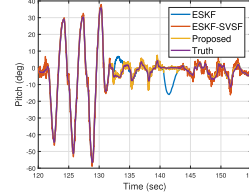


(c)

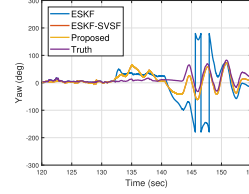
**FIGURE 12.** Attitude estimation results for Faulty Case 3 (Scenario 2): (a) roll, (b) pitch, and (c) yaw.



(a)



(b)



(c)

**FIGURE 13.** Attitude estimation results for Faulty Case 4 (Scenario 2): (a) roll, (b) pitch, and (c) yaw.

in the normal case, i.e., without fault injection. It can be seen from Fig. 9 that the ESKF estimation results are closer to the true attitude than the ESKF-SVFS results are. This finding confirms the optimality of the ESKF when the system and

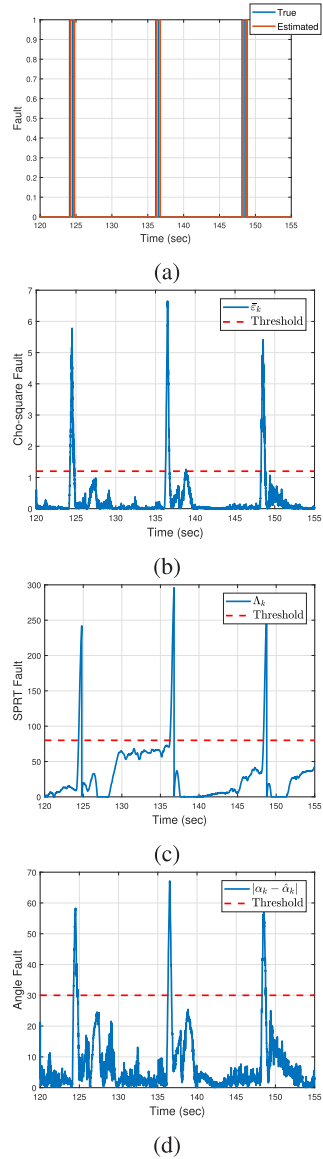


**FIGURE 14.** Fault detection result for Faulty Case 1 (Scenario 1): (a) true fault, (b) chi-square fault detection, (c) SPRT fault detection, and (d) angle deviation fault detection.

measurement models are accurate, with no modeling error [47]. However, the proposed ESKF-SVFS yields the same estimation result as the ESKF since it can switch to the ESKF when no system fault is detected. Specifically, as shown in Table 5, the estimation performance of the proposed ESKF is the same as that of the ESKF, which is better than that of the ESKF-SVFS without the comprehensive fault detection strategy for the normal case.

By contrast, Figs. 10 and 11 depict the attitude estimation results in Faulty Cases 1 and 2 (Scenario 1). The ESKF-SVFS algorithm yields better attitude estimation results, while the attitude estimates obtained with the ESKF significantly deviate from the true values during the fault injection time intervals at 124s, 136s, and 148s. It can similarly be observed from Figs. 12 and 13 that in Faulty Cases 3

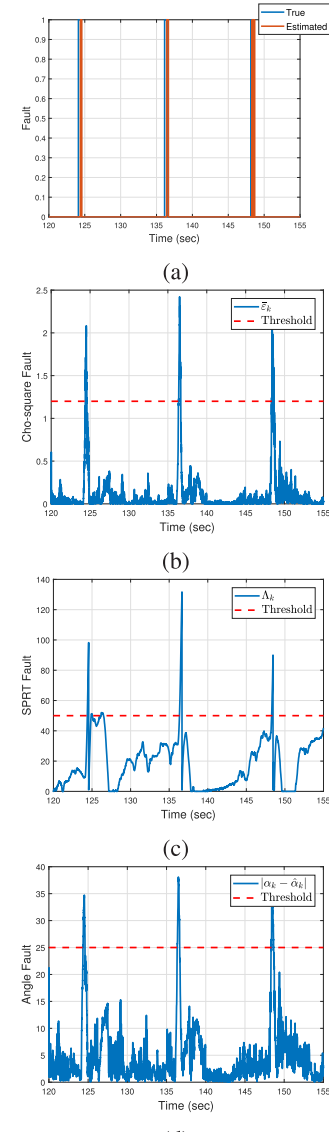


**FIGURE 15.** Fault detection result for Faulty Case 2 (Scenario 1): (a) true fault, (b) chi-square fault detection, (c) SPRT fault detection, and (d) angle deviation fault detection.

and 4 (Scenario 2), the estimation errors under the ESKF-SVFS algorithm are also much smaller, resulting in improved robustness. Thus, it can be concluded that although the estimation solution of the SVSF is not optimal, as shown in Fig. 9 for the case in which there is no system modeling discrepancy, it is apparently robust to modeling uncertainty.

In particular, the estimated yaw obtained via the ESKF severely deviates from the true yaw during times of fault injection, as shown in Figs. 10 and 11, whereas the estimated yaw obtained via the ESKF-SVFS algorithm closely follows the true yaw during these intervals. This severe yaw deviation might be due to the accumulation of roll and pitch angle error since the roll and pitch error will contribute to the calculation described in (14), thus yielding incorrect yaw predictions.

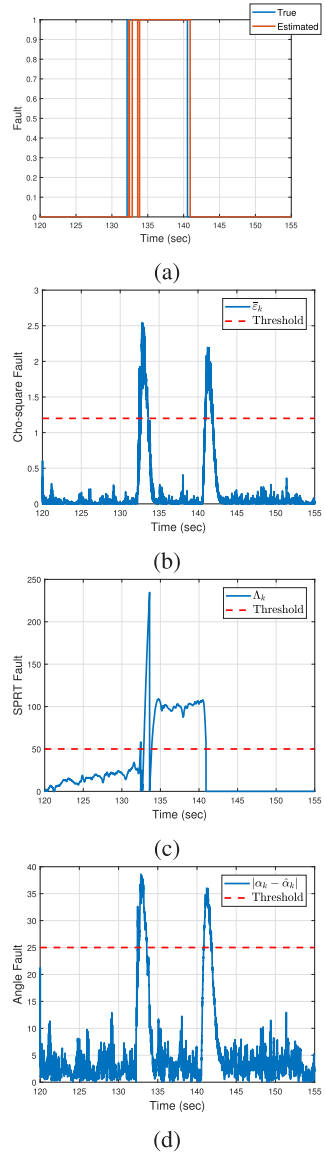


**FIGURE 16.** Fault detection result for Faulty Case 3 (Scenario 2): (a) true fault, (b) chi-square fault detection, (c) SPRT fault detection, and (d) angle deviation fault detection.

In addition, as shown in Figs. 10–13, the proposed ESKF outperforms the ESKF and the ESKF-SVFS without the comprehensive fault detection strategy for all four fault scenarios. This performance improvement of the proposed ESKF-SVFS can be attributed to the comprehensive fault detection scheme of accurate detection of system faults. Specifically, Figs. 14–17 show the fault diagnosis result, combining the fault detection of the chi-square, SPRT, and angle deviation based on Table 1. As shown in Figs. 14–15, the chi-square-based fault detection is sufficient for detecting the fast-growing fault in a short time, belonging to fault scenario 1. However, the chi-square fault detection is not suitable for detecting the constant-level fault in a relatively long time, but the SPRT can accurately detect such a fault, as shown in Figs. 16–17. Therefore, overall, the proposed fault detection

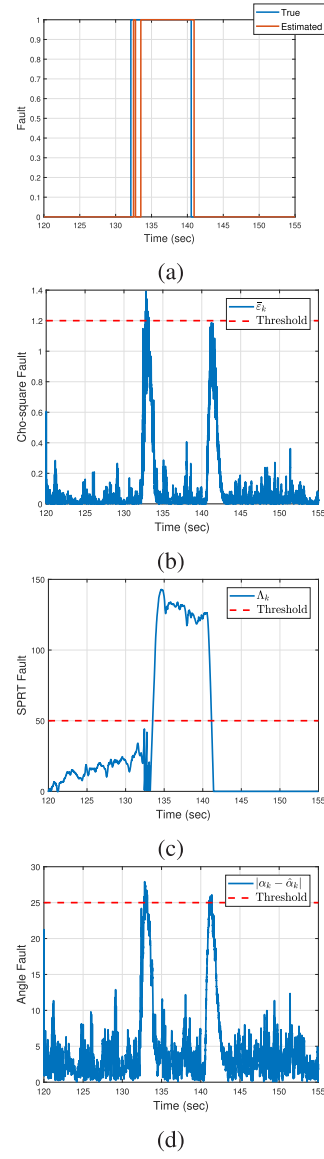


**FIGURE 17.** Fault detection result for Faulty Case 4 (Scenario 2): (a) true fault, (b) chi-square fault detection, (c) SPRT fault detection, and (d) angle deviation fault detection.

algorithm can accurately identify system faults in most cases, as shown in Figs. 14(a), 15(a), 16(a), and 17(a), although complete system fault detection is not always achievable. Based on the fault diagnosis result, the proposed ESKF-SVFS can switch to the ESKF for guaranteeing optimality when no fault is detected and to the SVSF for ensuring robustness when a fault is detected, resulting in a better estimation result.

Although the proposed ESKF-SVFS algorithm is robust to system modeling uncertainty, it also has a few disadvantages, as follows [24]: its computational complexity is slightly increased due to the introduction of the calculation of the SVSF gain, as shown in Table 6; a priori or application-specific information is needed to determine an appropriate fixed smoothing boundary layer width  $\psi$  (based on the noise statistics); and numerical errors may occur if the innovation

**TABLE 6.** Computation times for the ESKF, ESKF-SVSF, and proposed algorithms.

Computation Time (s)	ESKF	ESKF-SVSF	ESKF-SVSF (proposed)
Normal Case	5.3198	6.0750	7.2342
Faulty Case 1	6.3516	6.7553	7.3432
Faulty Case 2	5.2859	5.9215	7.1294
Faulty Case 3	5.7913	6.4046	7.3445
Faulty Case 4	5.2268	5.9815	6.4546

$e_{z,k}$  is exceedingly small and is not corrected (leading to division by zero when computing the SVSF gain as given in (39)). Note that the estimation result of the SVSF-VBL [24] is not presented in this paper since the computation of  $\psi$  in (47) often leads to numerical error due to the division by zero.

## VI. CONCLUSION

Attitude estimation that is robust to modeling uncertainty is crucial for the safe and reliable navigation of UAVs. This paper proposes a novel robust attitude estimation algorithm based on the ESKF and SVSF algorithms. The accuracy of an ESKF and the robustness of the SVSF are effectively combined to achieve improved attitude estimation, resulting in a novel robust attitude estimation algorithm called the ESKF-SVSF algorithm.

The proposed ESKF-SVSF algorithm has been validated on experimental data collected from a small UAV in the presence of modeling uncertainty, and its performance has been compared with that of the ESKF approach. In this experiment, two types of fault bias signals were intentionally injected into the raw gyroscope signals to simulate modeling uncertainty. Fault bias often occurs when a UAV experiences excessive vibration or in the case of a faulty IMU and causes the filter results to diverge from the actual operation state.

The experimental results demonstrate that the proposed ESKF-SVSF algorithm greatly improves the accuracy of state estimation in the presence of a small bias compared with the conventional ESKF algorithm when modeling error arises due to IMU faults. In particular, the proposed comprehensive fault detection scheme combining different methods was able to accurately detect the system fault. Based on the fault diagnosis, the proposed ESKF-SVSF not only guarantees the optimality of the ESKF but also the robustness of the SVSF. Future work will focus on combining the results of the ESKF and ESKF-SVSF algorithms using multimodel filtering approaches. This will allow the optimality of the ESKF to be maintained during fault-free operation while preserving the robustness of the ESKF-SVSF algorithm in the case of fault occurrence.

## REFERENCES

- [1] H. No, A. Cho, and C. Kee, "Attitude estimation method for small UAV under accelerative environment," *GPS Solutions*, vol. 19, no. 3, pp. 343–355, Jul. 2015.
- [2] Z. Wu, M. Yao, H. Ma, W. Jia, and F. Tian, "Low-cost antenna attitude estimation by fusing inertial sensing and two-antenna GPS for vehicle-mounted satcom-on-the-move," *IEEE Trans. Veh. Technol.*, vol. 62, no. 3, pp. 1084–1096, Mar. 2013.
- [3] M. T. Sabet, H. M. Daniali, A. Fathi, and E. Alizadeh, "A low-cost dead reckoning navigation system for an AUV using a robust AHRS: Design and experimental analysis," *IEEE J. Ocean. Eng.*, vol. 43, no. 4, pp. 927–939, Oct. 2018.
- [4] L. Cao, D. Qiao, H. Lei, and G. Wang, "Strong tracking sigma point predictive variable structure filter for attitude synchronisation estimation," *J. Navigat.*, vol. 71, no. 3, pp. 607–624, May 2018.
- [5] L. Cao, Y. Chen, Z. Zhang, H. Li, and A. K. Misra, "Predictive smooth variable structure filter for attitude synchronization estimation during satellite formation flying," *IEEE Trans. Aerosp. Electron. Syst.*, vol. 53, no. 3, pp. 1375–1383, Jun. 2017.
- [6] L. Cao and H. Li, "Unscented predictive variable structure filter for satellite attitude estimation with model errors when using low precision sensors," *Acta Astron.*, vol. 127, no. 3, pp. 505–513, Oct./Nov. 2016.
- [7] P. Lu, E. van Kampen, C. C. de Visser, and Q. P. Chu, "Framework for simultaneous sensor and actuator fault-tolerant flight control," *J. Guid., Control, Dyn.*, vol. 40, no. 8, pp. 2133–2136, Jun. 2017.
- [8] P. Lu, E.-J. van Kampen, C. de Visser, and Q. Chu, "Nonlinear aircraft sensor fault reconstruction in the presence of disturbances validated by real flight data," *Control Eng. Pract.*, vol. 49, pp. 112–128, Apr. 2016.
- [9] J. Wu, Z. Zhou, B. Gao, R. Li, Y. Cheng, and H. Fourati, "Fast linear quaternion attitude estimator using vector observations," *IEEE Trans. Automat. Sci. Eng.*, vol. 15, no. 1, pp. 307–319, Jan. 2018.
- [10] J. Wu, Z. Zhou, J. Chen, H. Fourati, and R. Li, "Fast complementary filter for attitude estimation using low-cost MARG sensors," *IEEE Sensors J.*, vol. 16, no. 18, pp. 6997–7007, Sep. 2016.
- [11] R. Costanzo, F. Fanelli, N. Monni, A. Ridolfi, and B. Allotta, "An attitude estimation algorithm for mobile robots under unknown magnetic disturbances," *IEEE/ASME Trans. Mechatronics*, vol. 21, no. 4, pp. 1900–1911, Aug. 2016.
- [12] J. K. Lee, E. J. Park, and S. N. Robinovitch, "Estimation of attitude and external acceleration using inertial sensor measurement during various dynamic conditions," *IEEE Trans. Instrum. Meas.*, vol. 61, no. 8, pp. 2262–2273, Aug. 2012.
- [13] H. Zhao and Z. Wang, "Motion measurement using inertial sensors, ultrasonic sensors, and magnetometers with extended Kalman filter for data fusion," *IEEE Sensors J.*, vol. 12, no. 5, pp. 943–953, May 2012.
- [14] Y. S. Suh, "Orientation estimation using a quaternion-based indirect Kalman filter with adaptive estimation of external acceleration," *IEEE Trans. Instrum. Meas.*, vol. 59, no. 12, pp. 3296–3305, Dec. 2010.
- [15] D. Titterton, J. L. Weston, and J. Weston, *Strapdown Inertial Navigation Technology*, vol. 17. Stevenage, U.K.: IET, 2004.
- [16] A. M. Sabatini, "Quaternion-based extended Kalman filter for determining orientation by inertial and magnetic sensing," *IEEE Trans. Biomed. Eng.*, vol. 53, no. 7, pp. 1346–1356, Jul. 2006.
- [17] W. Li and J. Wang, "Effective adaptive Kalman filter for MEMS-IMU/magnetometers integrated attitude and heading reference systems," *J. Navigat.*, vol. 66, no. 1, pp. 99–113, 2013.
- [18] N. Yadav and C. Bleakley, "Accurate orientation estimation using AHRS under conditions of magnetic distortion," *Sensors*, vol. 14, no. 11, pp. 20008–20024, Jan. 2014.
- [19] C. W. Kang, H. J. Kim, and C. G. Park, "A human motion tracking algorithm using adaptive EKF based on Markov chain," *IEEE Sensors J.*, vol. 16, no. 24, pp. 8953–8962, Dec. 2016.
- [20] J. Marzat, H. Piet-Lahanier, F. Damongeot, and E. Walter, "Model-based fault diagnosis for aerospace systems: A survey," *Proc. Inst. Mech. Eng., G, J. Aerosp. Eng.*, vol. 226, no. 10, pp. 1329–1360, 2012.
- [21] H. Alwi and C. Edwards, "Robust fault reconstruction for linear parameter varying systems using sliding mode observers," *Int. J. Robust Nonlinear Control*, vol. 24, no. 14, pp. 1947–1968, Sep. 2014.
- [22] P. Lu and E.-J. Van Kampen, "Aircraft inertial measurement unit fault identification with application to real flight data," in *Proc. AIAA Guid., Navigat., Control Conf.*, Kissimmee, FL, USA, 2015, p. 0859.
- [23] K. H. Kim, J. G. Lee, and C. G. Park, "Adaptive two-stage extended Kalman filter for a fault-tolerant INS-GPS loosely coupled system," *IEEE Trans. Aerosp. Electron. Syst.*, vol. 45, no. 1, pp. 125–137, Jan. 2009.
- [24] S. A. Gadsden, S. Habibi, and T. Kirubarajan, "Kalman and smooth variable structure filters for robust estimation," *IEEE Trans. Aerosp. Electron. Syst.*, vol. 50, no. 2, pp. 1038–1050, Apr. 2014.
- [25] S. A. Gadsden, M. Al-Shabi, I. Arasaratnam, and S. R. Habibi, "Combined cubature Kalman and smooth variable structure filtering: A robust nonlinear estimation strategy," *Signal Process.*, vol. 96, pp. 290–299, Mar. 2014.

- [26] S. A. Gadsden, Y. Song, and S. R. Habibi, "Novel model-based estimators for the purposes of fault detection and diagnosis," *IEEE/ASME Trans. Mechatronics*, vol. 18, no. 4, pp. 1237–1249, Aug. 2013.
- [27] R. Wang, Z. Xiong, J. Liu, J. Xu, and L. Shi, "Chi-square and SPRT combined fault detection for multisensor navigation," *IEEE Trans. Aerosp. Electron. Syst.*, vol. 52, no. 3, pp. 1352–1365, Jun. 2016.
- [28] C. Yang, A. Mohammadi, and Q.-W. Chen, "Multi-sensor fusion with interacting multiple model and chi-square test tolerant filter," *Sensors*, vol. 16, no. 11, p. 1835, Nov. 2016.
- [29] T. S. Bruggemann, D. G. Greer, and R. A. Walker, "GPS fault detection with IMU and aircraft dynamics," *IEEE Trans. Aerosp. Electron. Syst.*, vol. 47, no. 1, pp. 305–316, Jan. 2011.
- [30] V. Madyastha, V. Ravindra, S. Mallikarjunan, and A. Goyal, "Extended Kalman filter vs. error state Kalman filter for aircraft attitude estimation," in *Proc. AIAA Guid., Navigat., Control Conf.*, Portland, OR, USA, 2011, p. 6615.
- [31] N. Trawny and S. I. Roumeliotis, "Indirect Kalman filter for 3D attitude estimation," Dept. Comp. Sci. Eng., Univ. Minnesota, Tech. Rep. 2005-002, 2005.
- [32] A. Santamaría-Navarro, G. Loianno, J. Solà, V. Kumar, and J. Andrade-Cetto, "Autonomous navigation of micro aerial vehicles using high-rate and low-cost sensors," *Auton. Robots*, vol. 42, no. 6, pp. 1263–1280, Aug. 2018.
- [33] F. L. Markley, "Attitude error representations for Kalman filtering," *J. Guid., Control, Dyn.*, vol. 26, no. 2, pp. 311–317, Mar. 2003.
- [34] A. Makni, H. Fourati, and A. Y. Kibangou, "Energy-aware adaptive attitude estimation under external acceleration for pedestrian navigation," *IEEE/ASME Trans. Mechatronics*, vol. 21, no. 3, pp. 1366–1375, Jun. 2016.
- [35] S. Weiss, M. W. Achtelik, S. Lynen, M. C. Achtelik, L. Kneip, M. Chli, and R. Siegwart, "Monocular vision for long-term micro aerial vehicle state estimation: A compendium," *J. Field Robot.*, vol. 30, no. 5, pp. 803–831, Aug. 2013.
- [36] G. Zhang and L.-T. Hsu, "Intelligent GNSS/INS integrated navigation system for a commercial UAV flight control system," *Aerosp. Sci. Technol.*, vol. 80, pp. 368–380, Sep. 2018.
- [37] J. L. Crassidis and J. L. Junkins, *Optimal Estimation of Dynamic Systems*. Boca Raton, FL, USA: Chapman & Hall, 2004.
- [38] S. Habibi, "The smooth variable structure filter," *Proc. IEEE*, vol. 95, no. 5, pp. 1026–1059, May 2007.
- [39] L. Cao, J. Li, L. Han, and H. Li, "Adaptive predictive variable structure filter for attitude synchronization estimation," *J. Navigat.*, vol. 70, no. 1, pp. 205–223, Jan. 2017.
- [40] L. Cao, D. Ran, X. Chen, X. Li, and B. Xiao, "Huber second-order variable structure predictive filter for satellites attitude estimation," *Int. J. Control., Automat. Syst.*, vol. 17, no. 7, pp. 1781–1792, Jul. 2019.
- [41] S. A. Gadsden and A. S. Lee, "Advances of the smooth variable structure filter: Square-root and two-pass formulations," *J. Appl. Remote Sens.*, vol. 11, no. 1, Mar. 2017, Art. no. 015018.
- [42] M. A. Al-Shabi, "The general toeplitz/observability smooth variable structure filter," Ph.D. dissertation, Dept. Mech. Eng., McMaster Univ., Hamilton, ON, Canada, 2011.
- [43] W. Youn and H. Myung, "Robust interacting multiple model with modeling uncertainties for maneuvering target tracking," *IEEE Access*, vol. 7, no. 1, pp. 65427–65443, 2019.
- [44] J. M. Goodman, S. A. Wilkerson, C. Eggleton, and S. A. Gadsden, "A multiple model adaptive SVSF-KF estimation strategy," *Proc. SPIE*, vol. 50, no. 2, pp. 11018–11030, May 2019.
- [45] W. W. Piegorsch and W. J. Padgett, "Sequential probability ratio test," in *International Encyclopedia of Statistical Science*, M. Lovric, Ed. Berlin, Germany: Springer, May 2014, pp. 1305–1308.
- [46] Y. Huang, Y. Zhang, P. Shi, Z. Wu, J. Qian, and J. A. Chambers, "Robust Kalman filters based on Gaussian scale mixture distributions with application to target tracking," *IEEE Trans. Syst., Man, Cybern. Syst.*, vol. 49, no. 10, pp. 2082–2096, Oct. 2019. doi: [10.1109/TSMC.2017.2778269](https://doi.org/10.1109/TSMC.2017.2778269).
- [47] S. A. Gadsden, "Smooth variable structure filtering: Theory and applications," Ph.D. dissertation, Dept. Mech. Eng., McMaster Univ., Hamilton, ON, Canada, 2011.



**WONKEUN YOUN** received the B.S. degree from Handong Global University, Pohang, South Korea, in 2008, and the M.S. degree from the Korea Advanced Institute of Science and Technology (KAIST), Daejeon, South Korea, in 2010, where he is currently pursuing the Ph.D. degree with the Department of Robotics.

He has been a Senior Researcher with the UAV System Division of the Korea Aerospace Research Institute (KARI), since 2011. His current research interests include multisensor fusion, Bayesian estimation theory, multimodal target tracking, and GPS/INS-based UAV navigation.



**STEPHEN ANDREW GADSDEN** (M'09–SM'19) received the Ph.D. degree in state and parameter estimation theory from McMaster University, Hamilton, ON, Canada, in 2011.

He was an Assistant Professor with the Department of Mechanical Engineering, University of Maryland, Baltimore, MD, USA, from 2014 to 2016. He is currently an Associate Professor with the College of Engineering and Physical Sciences, University of Guelph, Guelph, ON, Canada. His

work involves the optimal realization and further advancement of robust filtering strategies with applications in mechatronics and aerospace technology. He has a broad research background that includes the consideration of state and parameter estimation strategies, variable structure theory, fault detection and diagnosis, mechatronics, target tracking, cognitive systems, and artificial intelligence.

He is an elected Fellow of ASME, and a Professional Engineer of Ontario. He is a 2019 SPIE Rising Researcher award winner based on his work in intelligent estimation theory and is also a 2018 Ontario Early Researcher (ERA) award winner based on his work in intelligent condition monitoring strategies.

• • •